Supplementary Information (SI) for Materials Chemistry Frontiers.
This journal is © the Partner Organisations 2024

SUPPLEMENTARY MATERIAL

Fine-tuning of core-shell 1D nanoparticles for thermally conductive, yet electrically insulating, 3D-printable polymer nanocomposites

*Antoine Bodin, Thomas Pietri, Caroline Celle, Jean-Pierre Simonato**

AUTHOR ADDRESS

Univ. Grenoble Alpes, CEA, LITEN, F-38000 Grenoble, France

Synthesis of AgNW@SiO_2 core-shell nanostructures

Typically, 0.2 g of AgNWs were dispersed in 100 mL of absolute ethanol and magnetically stirred for 30 min at room temperature. Then, the appropriate amount of TEOS (0.325 %, 0.65 %, 1.30 %, 2.00 % or 4.00 % v/v to absolute ethanol), 3.3 mL of NH4OH and deionized water (1:1 vol% to TEOS) were successively added to the mixture under continuous stirring. The mixture was left under stirring for 15 h at room temperature. The reaction mixture was then vacuum filtered and washed several times with absolute ethanol on a 1.2 µm pore size PTFE membrane to get rid of free silica nanoparticles. The wet cake of AgNW@SiO2 was quickly redispersed in absolute ethanol for storage or in chloroform for further incorporation into the polymer matrix.

Preparation of PC-AgNW@SiO_2 bulk nanocomposites

PC was dissolved in chloroform (1 h stirring at room temperature), then the associated amount of the AgNWs@SiO2/CHCl3 solution was incorporated into the PC/CHCl3 solution and stirred for 30 min. Finally, the excess of CHCl3 was removed using a rotary evaporator. The resulting dry nanocomposite flakes were left one night under a fume hood for an additional drying. PC-AgNW@SiO2 nanocomposite flakes were then used to produce bulk samples (disk-shaped, 12.7 mm diameter, 1.2 mm thickness).

Shaping PC-AgNW@SiO_2 nanocomposites in filament form

Nanocomposite material for filament preparation was obtained from solution mixing as described previously. The nanocomposite flakes were firstly hot-pressed to get homogeneous nanocomposite slabs. Subsequently, these slabs were shredded in small pieces in preparation for the extrusion process. Before filament fabrication and 3D printing, all materials were put in an oven set at 120 °C for 3h to prevent moisture contamination. Neat PC and nanocomposite filaments were obtained through an extrusion-spooling process performed on a NEXT filament extruder from 3Devo, Netherlands. Process parameters were adjusted to fabricate a filament diameter of 1.75 ± 0.10 mm, as recorded by the laser diameter sensors. The optimal temperatures T1, T2, T3 and T4 from the hopper to the die along the extrusion barrel were respectively set at 215 °C, 220 °C, 240 °C and 240 °C for neat PC and 215 °C, 230 °C, 250 °C and 250 °C for the nanocomposite filament.

3D printing of neat PC and PC-AgNW@SiO_2 nanocomposite filaments

The best print head temperatures were found to be 250 °C for neat PC and 270 °C for the PC-AgNW@SiO_2 nanocomposite. The factory print bed was covered by a flat and leveled glass plate topped with a Buildtak™ standard printing surface. Prior to any new construction, the printing surface was coated with an adhesion-promoting primer (DimaFix™ spray) to enhance adhesion of the first layers and to avoid warping. The print bed was then maintained at 120 °C during the whole printing process. Concerning printing parameters, the printing nozzle had a diameter of 0.4 mm, the first layer height was set to 0.28 mm to ensure good part adhesion while normal layer heights were set to 0.15 mm. 3D test specimen were then printed as 30 x 30 x 1.5 mm squares with a 100 % rectilinear infill with various raster angles of 0°/90° (criss-crossed) or 0°/0° (unidirectional). Following successful printing, 12.7 mm-diameter disk-shaped samples were punched from those 3D printed test specimen for through-plane and in-plane thermal conductivity measurements.

Characterization

Silver Titration

Inductively coupled plasma – optical emission spectrometry (ICP-OES, 725 Series, Agilent Technologies, USA) was used to titrate silver after dissolution of the products in diluted nitric acid. To ensure good dissolution of the Ag core, all test samples were firstly sonicated at high power for several hours in concentrated HNO3 to break SiO2 shells.

Sample Imaging

The morphology of AgNWs and AgNW@SiO2 was observed using a field-emission - scanning electron microscope (FE-SEM, LEO 1530 VP Gemini, Zeiss, Germany) at accelerating voltages of 5kV and 10kV. FE-SEM samples were prepared by placing a drop of the AgNWs or AgNW@SiO2 solution on a small aluminum lid, then quickly dried on a hot plate to evaporate the residual solvent. The dispersion of AgNWs and AgNW@SiO2 inside the polycarbonate matrix was also studied by FE-SEM on bulk and 3D printed nanocomposite fracture surfaces. Before any observation, all samples were metalized by platinum sputtering. Diameters and lengths of AgNWs and AgNW@SiO2 nanoparticles were measured using the digital image processing software ImageJ. Elemental composition and mappings were obtained by energy dispersive X-ray spectroscopy (EDX, XFlash Detector 5030, Bruker, Germany).

FTIR Spectroscopy

Infrared spectra of AgNWs and AgNW@SiO2 samples were obtained with a Fourier transform infrared (FTIR) apparatus used in transmission mode (Vertex 70, Bruker Optics, Germany). In a typical analysis, a spatula tip amount of AgNWs or AgNW@SiO2 powder was mixed with KBr grinded crystals and disk-shaped under a uniaxial hydraulic press. All KBr samples were dried in an oven set at 80 °C before any FTIR analysis to avoid water contamination.

XPS Analysis

X-ray photoelectron spectra of AgNWs and AgNW@SiO2 were obtained with a X-ray photoelectron spectroscopy (XPS) apparatus (Versaprobe-II, Physical Electronics, USA).

Thermal Imaging

All samples were subjected to heating and cooling cycles while their surface temperature was recorded in real time with an infrared thermal camera (PI 450i, Optris, Germany). Heating was performed on a hot plate set at 100 °C and sample temperatures were monitored starting from room temperature for 90 s. For the cooling process, all samples were preheated beforehand and the initial time t0 was triggered as the samples were placed on a lab bench at room temperature to record their cooling performance.

Thermal Conductivity Measurements

Through-plane and in-plane thermal diffusivity measurements were performed on the disk-shaped samples using a laser flash apparatus at 25 °C, 50 °C, 75 °C, 100 °C and 125 °C (LFA447 NanoFlash, Netzsch, Germany). For in-plane measurements, the disk-shaped samples were cut into ≈ 1.2 mm-wide strips using a diamond-coated wire saw, rotated 90° and placed inside a square sample holder. Density values were measured in a 1 cm^3 cell with a He gas displacement pycnometry system at 25 °C (AccuPyc 1340, Micromeritics, USA). The average value was calculated from 25 successive measurements. Specific heat capacity was measured using a Microcalvet calorimeter (Setaram, France). Two measurements were carried out for each material. A thermal ramp fixed at a heating rate of 0.5 °C min^{-1} up to 125 °C was applied under air atmosphere after 1h of thermal stabilization at 20 °C.

Electrical Resistivity Measurements

Electrical resistivity was measured with a UR-SS probe mounted on a Hiresta-UX resistivity-meter for high resistivity samples (MCP-HT800, Mitsubishi Chemical Analytech, Japan).

Dielectric Measurements

Dielectric properties (dielectric constant, loss factor and electrical conductivity as a function of frequency) were measured using a Novocontrol Alpha-A impedance analyzer (Novocontrol, Germany) between 1 Hz and 1 MHz at 1 V (AC voltage), at room temperature. Two gold electrodes of 200 nm thickness and 5 mm diameter were sputtered onto each side of the samples (12.7 mm diameter). Only pure PC and the best-performing PC-AgNW@SiO2 nanocomposite were tested by dielectric spectroscopy.

Breakdown Voltage Measurements

Breakdown voltage was measured on 1 mm-thick samples using a Sefelec SXS-506 (Eaton, Ireland). Several tests were conducted for breakdown voltage measurements. The first test consisted in progressively increasing voltage from 0 to 6 kV for 60 s and recording the voltage at electrical breakdown. The second test, performed exclusively on the PC-AgNW@SiO2-20 nanocomposite, consisted in increasing voltage from 0 to [1, 2, 2.5 and 2.3 kV] for 10 s, followed by a 30 s hold. The elapsed time before electrical breakdown was then recorded.

Rheological Measurements

Rheological measurements were performed on a parallel plates rheometer (Kinexus Pro+, Netzsch, Germany) in oscillation mode, mounted with a 20 mm-diameter upper plate. The measurement area was heated at 250 °C for all samples. Beforehand, strain amplitude sweeps from 0.01 % to 100 % strain were run at a fixed frequency of 1 Hz to determine the linear viscoelastic region (LVER) limit for each sample. Then, frequency sweeps from 0.1 Hz to 100 Hz were carried out at a fixed strain rate corresponding to the LVER limit identified previously for each specific sample.

Tensile Properties Measurements

Tensile mechanical properties of neat PC, PC-AgNWs and PC-AgNW@SiO2 nanocomposites were evaluated from testing bulk H2 tensile specimen (gauge length, width and thickness of 25 mm, 4 mm and 1.2 mm respectively) on a Syntax universal testing machine (3R, France) with a 1 kN load cell, at room temperature and at a crosshead speed of 3 mm/min. Five to six specimens were tested and the test results were averaged and plotted into a single stress-strain curve for each batch of samples.

Thermal Stability Measurements

Mass loss percentage with increasing temperature was measured by thermogravimetric analysis (TGA) using a STA 449 from Netzsch, Germany. Two measurements were carried out for each material. A heating rate of 5 °C min-1 up to 800 °C was applied under air atmosphere.

Choosing the optimal AgNW@SiO_2 loading ratio for the PC-AgNW@SiO_2 study

Thermal conductivity, specific heat capacity and rheological properties were measured on PC-AgNW reference composite at 0.5, 1, 3, 5 and 7 vol% loading ratios. Thermal conductivity was improved, and the 3 vol% AgNW loading ratio exhibited a thermal conductivity value at the edge of the thermal percolation threshold (**Fig. S7a**). At the same time, specific heat capacity curves exhibited a transitional behavior around 3 vol%, with a gradual decrease in specific heat capacity value with increasing loading ratios (**Fig. S7b**). Finally, the rheological behavior significantly changed above 3 vol% loading as it can be observed on **Fig. S7c** where the linear viscoelastic region limit appeared sooner with a more defined G' drop. The viscosity of the melted PC-AgNWs nanocomposites gradually increased with filler loading, and would be too high to ensure a good processability in FDM 3D printing beyond 3 vol% loading (**Fig. S7d**). This preliminary study on PC-AgNWs nanocomposites revealed that the 3 vol% loading rate was the critical pivotal rate, providing the best trade-off between performance and processability. For this reason, the development of PC-AgNW@SiO2 nanocomposites was then carried out using a 3 vol% filler loading.

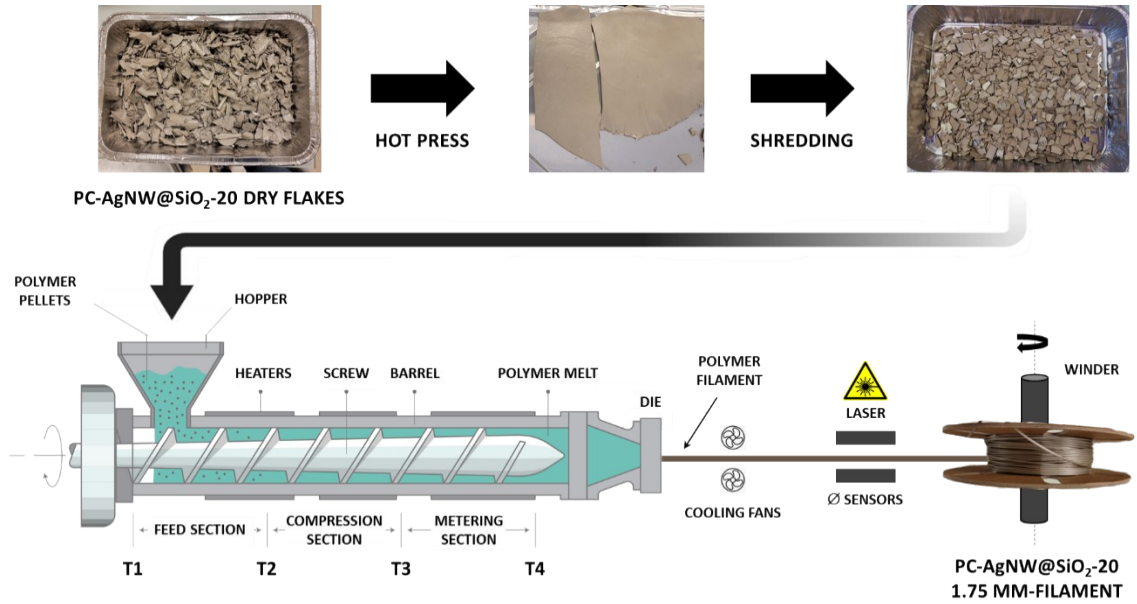

Fig. S1. PC-AgNW@SiO_2 nanocomposite filament shaping process

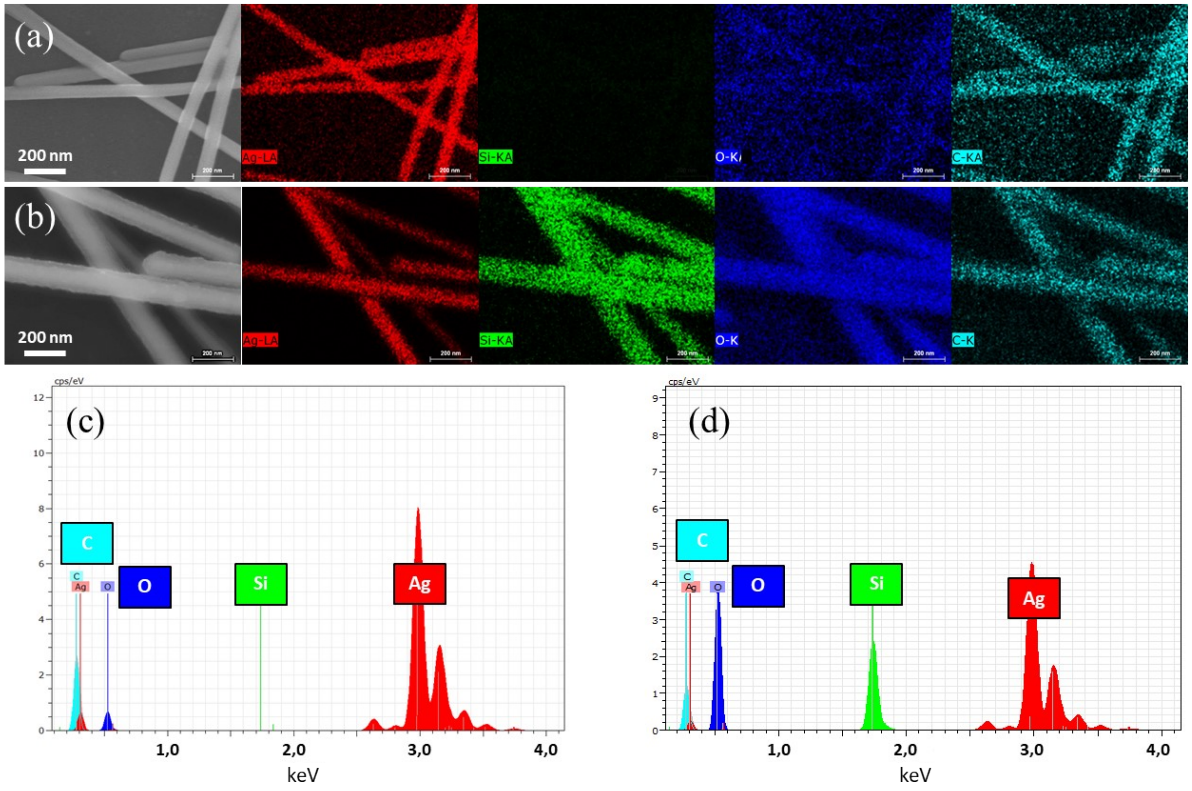

Fig. S2. EDX mappings of (a) pure AgNWs and (b) AgNW@SiO_2; EDX emission lines of (c) pure AgNWs and (d) AgNW@SiO_2.

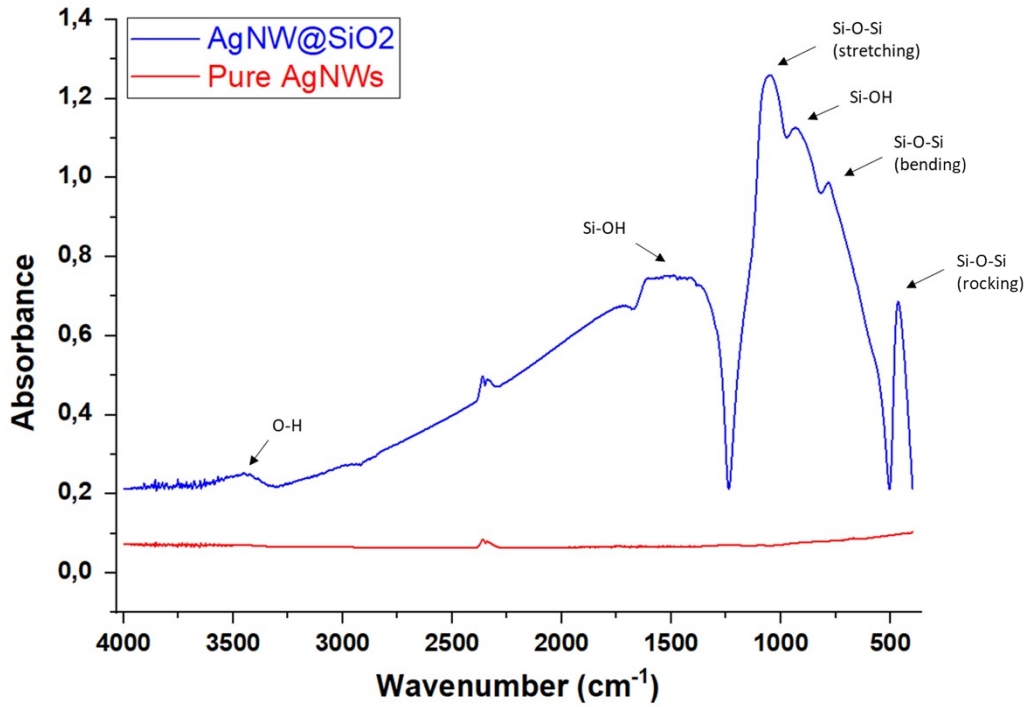

Fig. S3. FTIR spectra of pure AgNWs and AgNW@SiO_2 core-shell nanostructures. The indicated peaks in the AgNW@SiO_2 nanowires spectrum are those expected for silica.

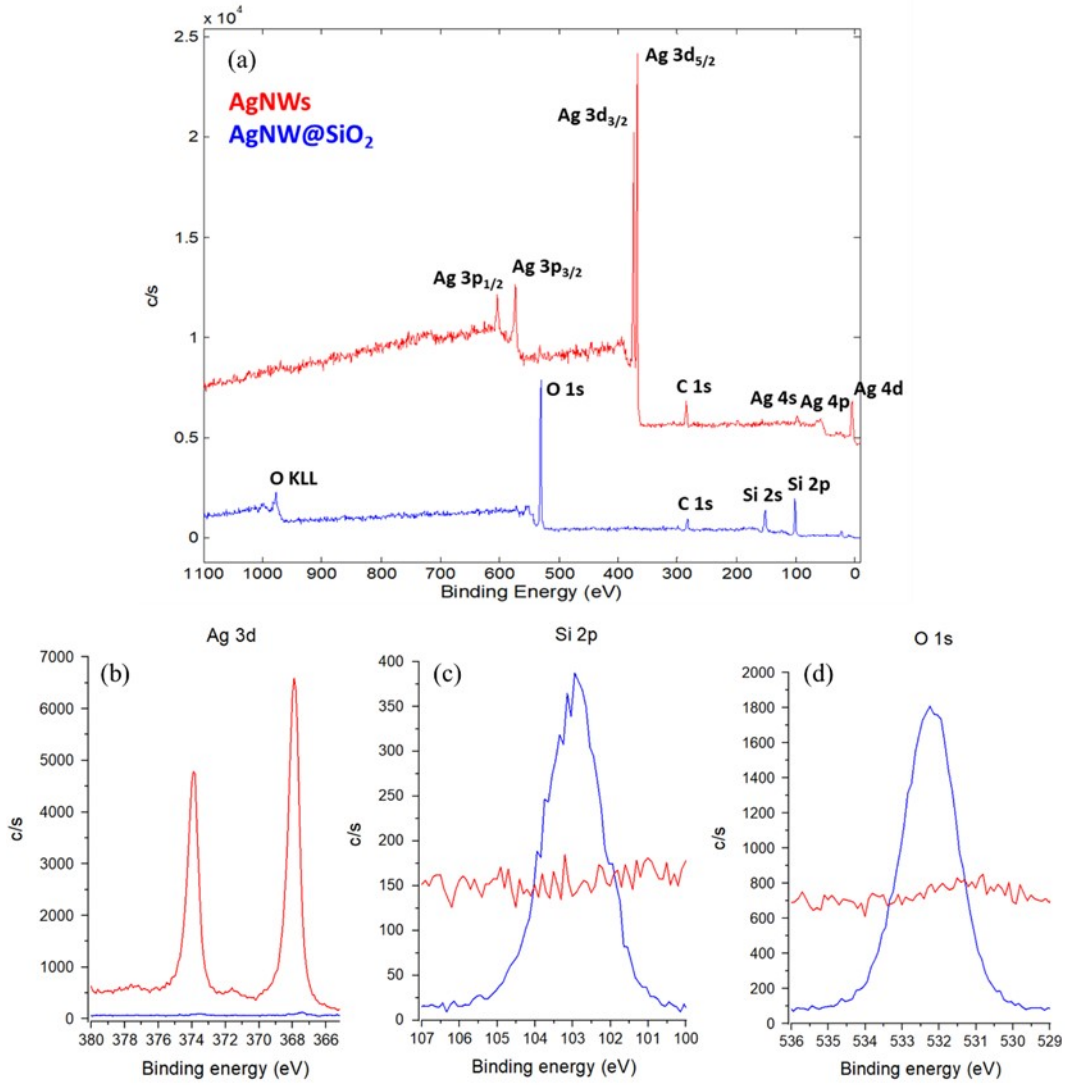

Fig. S4. XPS spectra of pure AgNWs and AgNW@SiO2: (a) broad XPS spectra. High-resolution XPS spectra of (b) Ag 3d scan, (c) Si 2p scan and (d) O 1s scan. The broad XPS spectrum of AgNWs is consistent and standard for silver nanoparticles and shows that AgNWs are clean, pure, and not oxidized. No traces of silver were found on the surface of the AgNW@SiO_2 core-shell nanowires, confirming the uniformity of the SiO_2 nanolayer around silver cores. The binding energies of the O 1s and the Si $2p_{3/2\text{-}1/2}$ narrow scans, with peaks measured at respectively 532.3 eV and 102.9 eV, are consistent with the presence of a uniform SiO_2 layer at the surface of AgNWs.

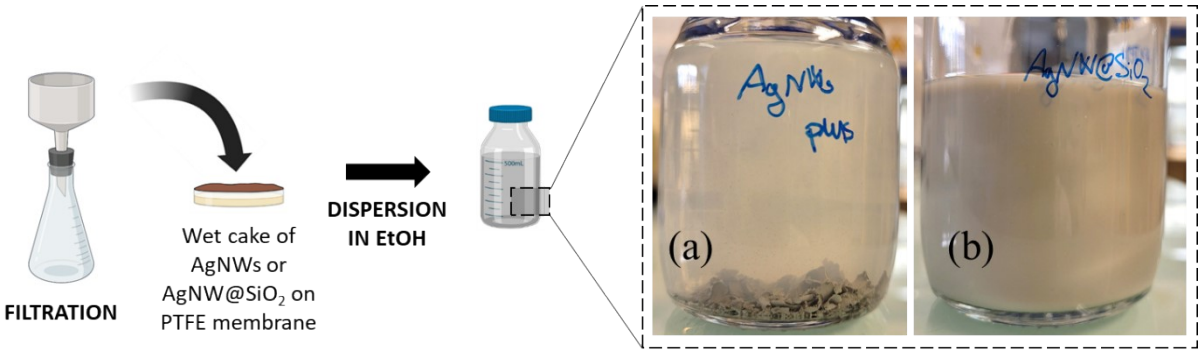

Fig. S5. Redispersion of (a) pure AgNWs and (b) AgNW@SiO_2 in ethanol after vacuum filtration.

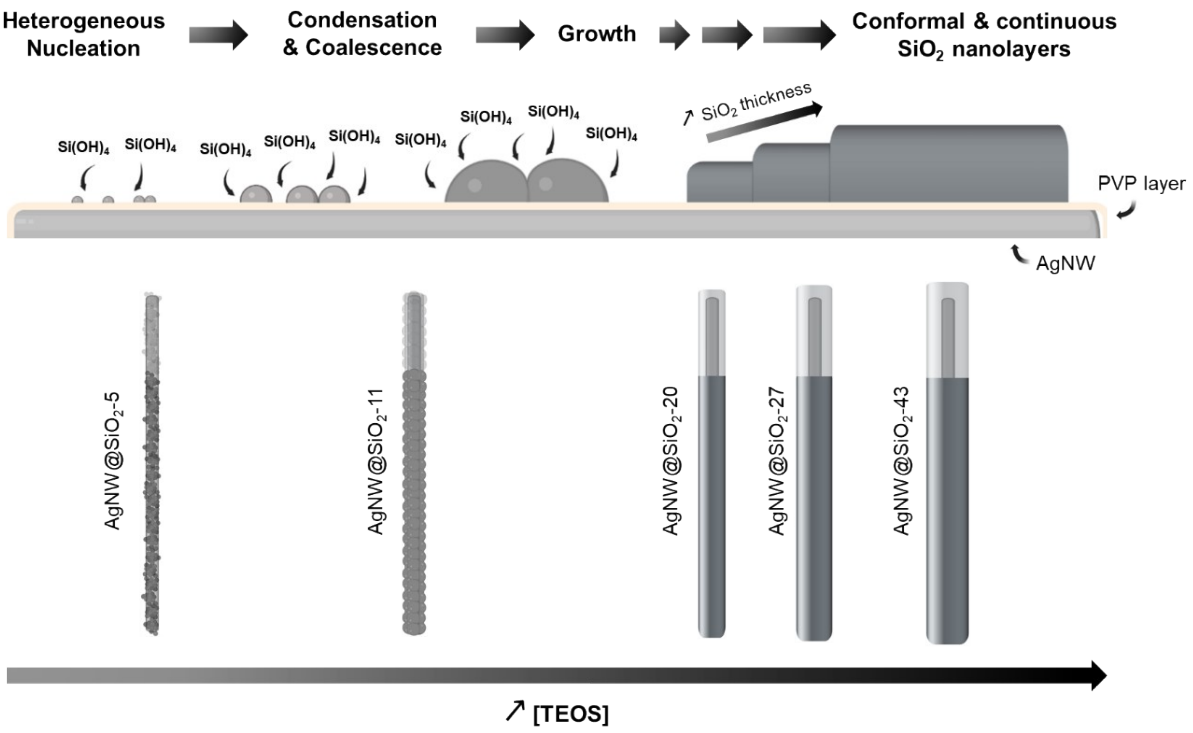

Fig. S6. Successive steps describing the formation of a conformal and continuous SiO_2 nanolayer at the surface of AgNW as a function of initial TEOS concentration.

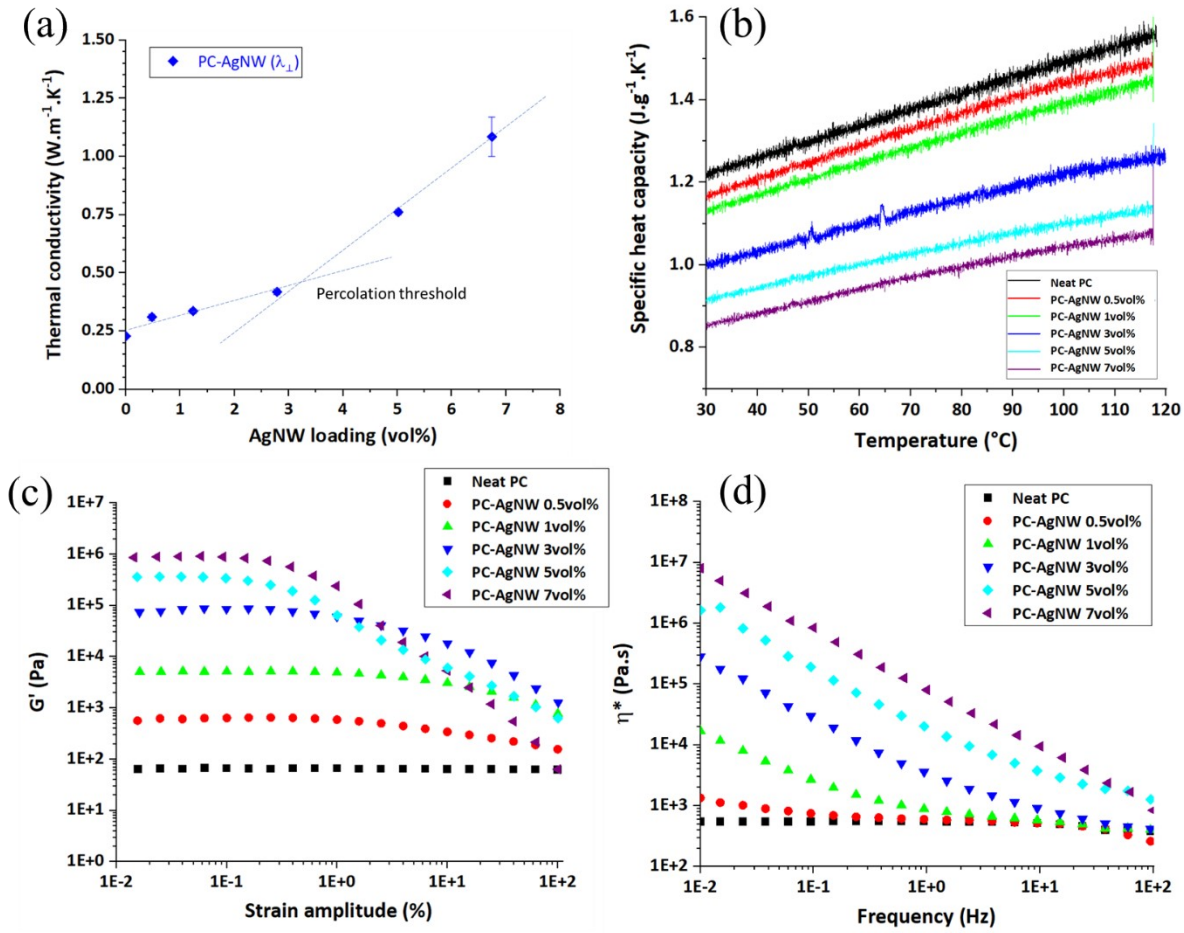

Fig. S7. (a) Thermal conductivity of PC-AgNWs nanocomposites as a function of the raw AgNW loading ratio. (b) Evolution of specific heat capacity of the PC-AgNWs nanocomposites with temperature. (c) Variation of the storage modulus G' as a function of strain amplitude of the PC-AgNWs nanocomposites, at 250 °C and 1 Hz. (d) Variation of the complex viscosity of the PC-AgNWs nanocomposites as a function of frequency at 250 °C.

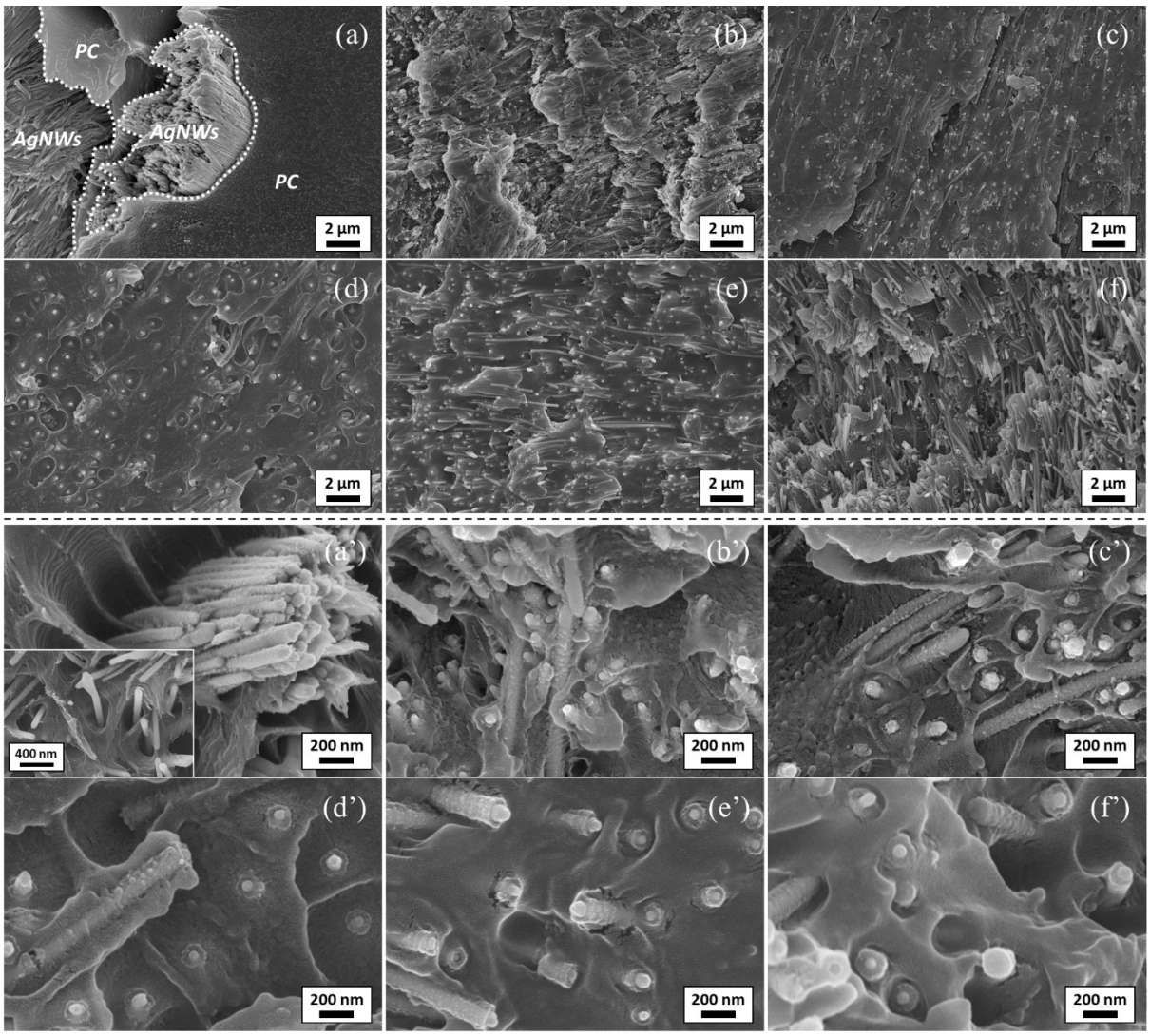

Fig. S8. FE-SEM images of fractured surfaces of (a,a') PC-AgNW, (b,b') PC-AgNW@SiO_2-5, (c,c') PC-AgNW@SiO_2-11, (d,d') PC-AgNW@SiO_2-20, (e,e') PC-AgNW@SiO_2-27 and (f,f') PC-AgNW@SiO_2-43 bulk samples.

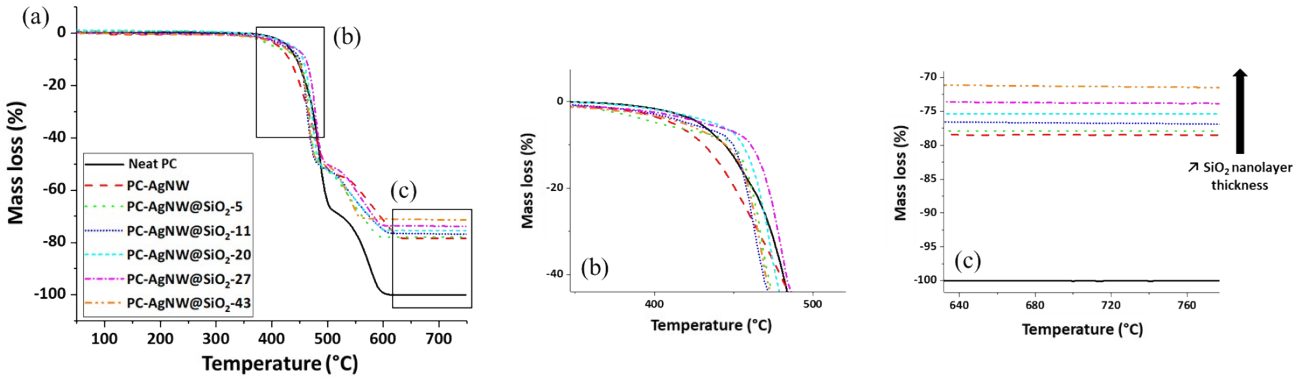

Fig. S9. TGA curves of neat PC and associated PC-AgNW@SiO_2 nanocomposites with varying SiO_2 shell thicknesses.

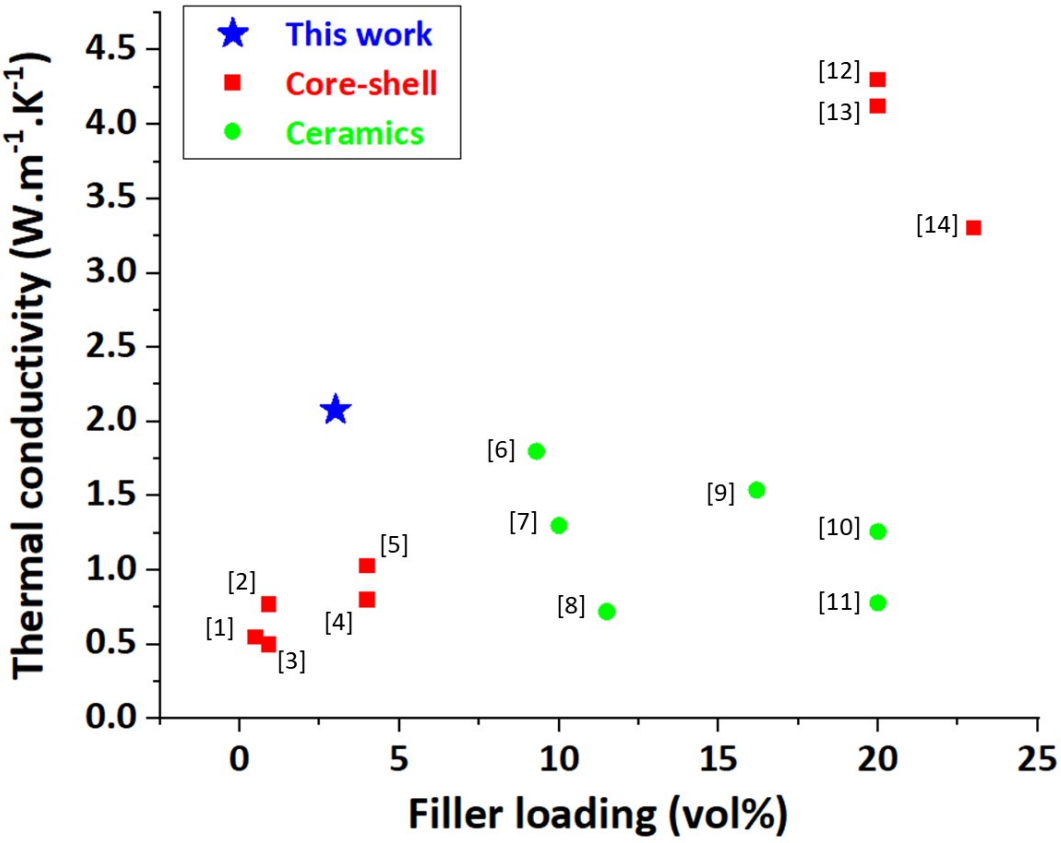

Fig. S10. Thermal conductivity values issued from the literature for thermally conductive and electrically insulating polymer nanocomposites filled with core-shell and ceramic fillers, compared to this work (blue star). References are the following:

[1] Wang Z-Y, Sun X, Wang Y, Liu J-D, Zhang C, Zhao Z-B, et al. Fabrication of high-performance thermally conductive and electrically insulating polymer composites with

siloxane/multi-walled carbon nanotube core-shell hybrids at low filler content. Polymer 2022;262:125430. https://doi.org/10.1016/j.polymer.2022.125430.

[2] Zhang L, Zhu W, Qi G, Li H, Qi D, Qi S. Highly Thermal Conductive and Electrically Insulating Epoxy Composites Based on Zinc-Oxide-Coated Silver Nanowires. Polymers 2022;14:3539. https://doi.org/10.3390/polym14173539.

[3] Shen C, Wang H, Zhang T, Zeng Y. Silica coating onto graphene for improving thermal conductivity and electrical insulation of graphene/polydimethylsiloxane nanocomposites. Journal of Materials Science & Technology 2019;35:36–43. https://doi.org/10.1016/j.jmst.2018.09.016.

[4] Jiang Y, Li M, Chen C, Xue Z, Xie X, Zhou X, et al. Effect of elastic modulus mismatch of epoxy/titanium dioxide coated silver nanowire composites on the performance of thermal conductivity. Composites Science and Technology 2018;165:206–13. https://doi.org/10.1016/j.compscitech.2018.06.028.

[5] Chen C, Tang Y, Ye YS, Xue Z, Xue Y, Xie X, et al. High-performance epoxy/silica coated silver nanowire composites as underfill material for electronic packaging. Composites Science and Technology 2014;105:80–5. https://doi.org/10.1016/j.compscitech.2014.10.002.

[6] Zhi C, Bando Y, Terao T, Tang C, Kuwahara H, Golberg D. Towards Thermoconductive, Electrically Insulating Polymeric Composites with Boron Nitride Nanotubes as Fillers. Advanced Functional Materials 2009;19:1857–62. https://doi.org/10.1002/adfm.200801435.

[7] Shimazaki Y, Hojo F, Takezawa Y. Preparation and characterization of thermoconductive polymer nanocomposite with branched alumina nanofiber. Appl Phys Lett 2008;92:133309. https://doi.org/10.1063/1.2907315.

[8] Zandieh A, Izadi H, Hamidinejad M, Shin H, Shi S, Martinez-Rubi Y, et al. Molecular engineering of the surface of boron nitride nanotubes for manufacture of thermally conductive dielectric polymer composites. Applied Surface Science 2022;587:152779. https://doi.org/10.1016/j.apsusc.2022.152779.

[9] Feng M, Pan Y, Zhang M, Gao Q, Liu C, Shen C, et al. Largely improved thermal conductivity of HDPE composites by building a 3D hybrid fillers network. Composites Science and Technology 2021;206:108666. https://doi.org/10.1016/j.compscitech.2021.108666.

[10] Özmıhçı FÖ, Balköse D. Effects of particle size and electrical resistivity of filler on mechanical, electrical, and thermal properties of linear low density polyethylene–zinc oxide composites. Journal of Applied Polymer Science 2013;130:2734–43. https://doi.org/10.1002/app.39433.

[11] Pietri T, Wiley BJ, Simonato J-P. Boron Nitride Nanotubes for Heat Dissipation in Polycaprolactone Composites. ACS Appl Nano Mater 2021;4:4774–80. https://doi.org/10.1021/acsanm.1c00365.

[12] Zhou Y, Liu F. High-performance polyimide nanocomposites with core-shell AgNWs@BN for electronic packagings. Appl Phys Lett 2016;109:082901. https://doi.org/10.1063/1.4961625.

[13] Zhou Y, Liu F, Chen C-Y. Use of BN-coated copper nanowires in nanocomposites with enhanced thermal conductivity and electrical insulation. Adv Compos Hybrid Mater 2019;2:46–50. https://doi.org/10.1007/s42114-019-00077-9.

[14] Noma Y, Saga Y, Une N. Amorphous silica-coated graphite particles for thermally conductive and electrically insulating resins. Carbon 2014;78:204–11. https://doi.org/10.1016/j.carbon.2014.06.073.

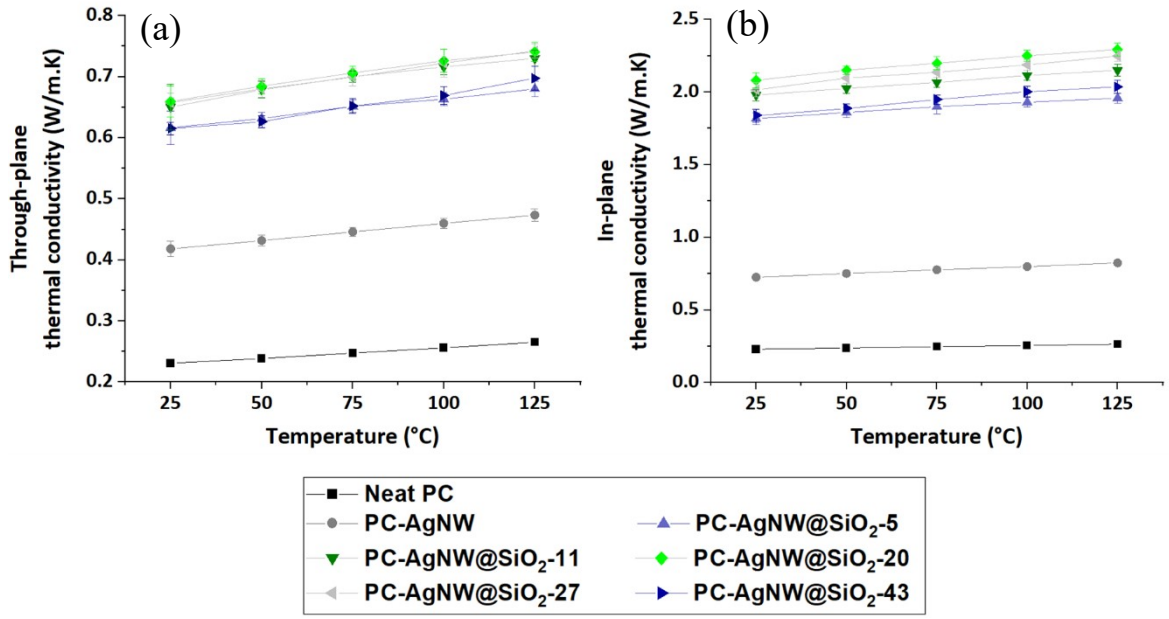

Fig. S11. Temperature dependence of (a) through-plane and (b) in-plane thermal conductivity of neat PC and PC-AgNW@SiO2 nanocomposites.

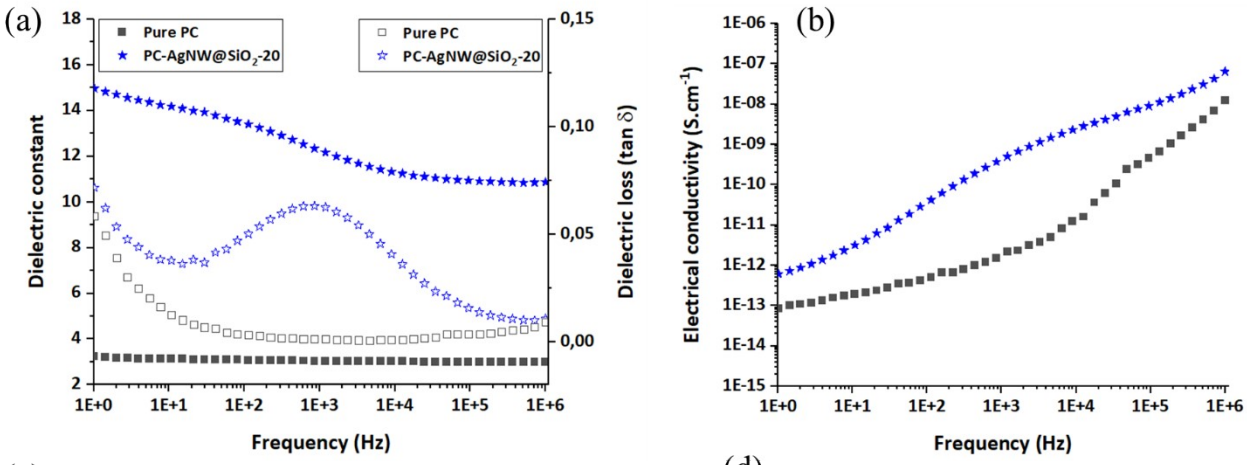

(c)

Sample	Voltage at electrical breakdown	Corresponding breakdown voltage
Pure PC	-	-
PC-AgNWs	< 1 V	< 0.001 kV.mm^{-1}
PC-AgNW@SiO_2	3.07 kV	3.07 kV.mm^{-1}

(d)

Voltage	Elapsed time before electrical breakdown for a 30 s hold *(After a 10 s voltage build-up)*
1 kV	-
2 kV	-
2.5 kV	4 s
2.3 kV	15 s

Fig. S12. (a) Evolution of the dielectric constant and dielectric losses of pure PC and PC-AgNW@SiO_2-20 as a function of frequency, at 25°C. (b) Evolution of the electrical conductivity of both samples as a function of frequency, at 25°C. (c) Results of the first test of electrical breakdown consisting of progressively increasing voltage from 0 to 6 kV for 60 s for pure PC, PC-AgNWs and PC-AgNW@SiO_2 samples. (d) Results of the second test of electrical breakdown, performed exclusively on the PC-AgNW@SiO_2-20 sample, consisting of increasing voltage from 0 to [1, 2, 2.5 and 2.3 kV] for 10 s, followed by a 30 s hold.

As expected, pure PC exhibited a low dielectric constant of around 3.0 throughout the whole frequency test range. By comparison, the PC-AgNW@SiO_2-20 sample exhibited a much higher dielectric constant, equal to 10.9 at 1 MHz, which increased at lower frequencies (12.2 at 1 kHz and 14.9 at 1 Hz). The addition of AgNW@SiO_2 nanofillers to the PC matrix creates a multitude of new interfaces within the nanocomposite. These interfaces are responsible for the phenomenon of interfacial polarization, which generally occurs in heterogeneous media when an accumulation of electrical charges takes place at the interfaces between the different

phases constituting the material. This interfacial polarization leads to an increase in the overall dielectric constant of the nanocomposite. As expected, pure PC exhibited low dielectric losses of the order of 0.01, increasing at low frequencies. Surprisingly, PC-AgNW@SiO_2-20 showed a marked dielectric relaxation around 1 kHz. This observation can be explained in various ways, although the interfacial polarization argument remains the most convincing. At the interface between the 1D-shaped AgNW@SiO_2 nanofillers and the PC matrix, zones of electric charge accumulation are created, and dipole moments form at the interfaces, resulting in increased dielectric losses due to possible short-range molecular displacements and reorientations in response to the applied alternating electric field. Furthermore, the electrical conductivity of pure PC and PC-AgNW@SiO_2-20 samples decreases with decreasing frequency (2.2×10^{-12} and 5.1×10^{-10} $S.cm^{-1}$ at 10 kHz, respectively, up to 8.5×10^{-14} and 6.1×10^{-13} $S.cm^{-1}$ at 1 Hz), which is not surprising for insulating materials.

On the other hand, the PC-AgNW@SiO_2 sample exhibited better electrical breakdown performance, confirming the beneficial effect of the SiO_2 shell on electrical performances of PC-AgNW@SiO_2 nanocomposites, which is in line with expectations for the nanostructures used in this work.

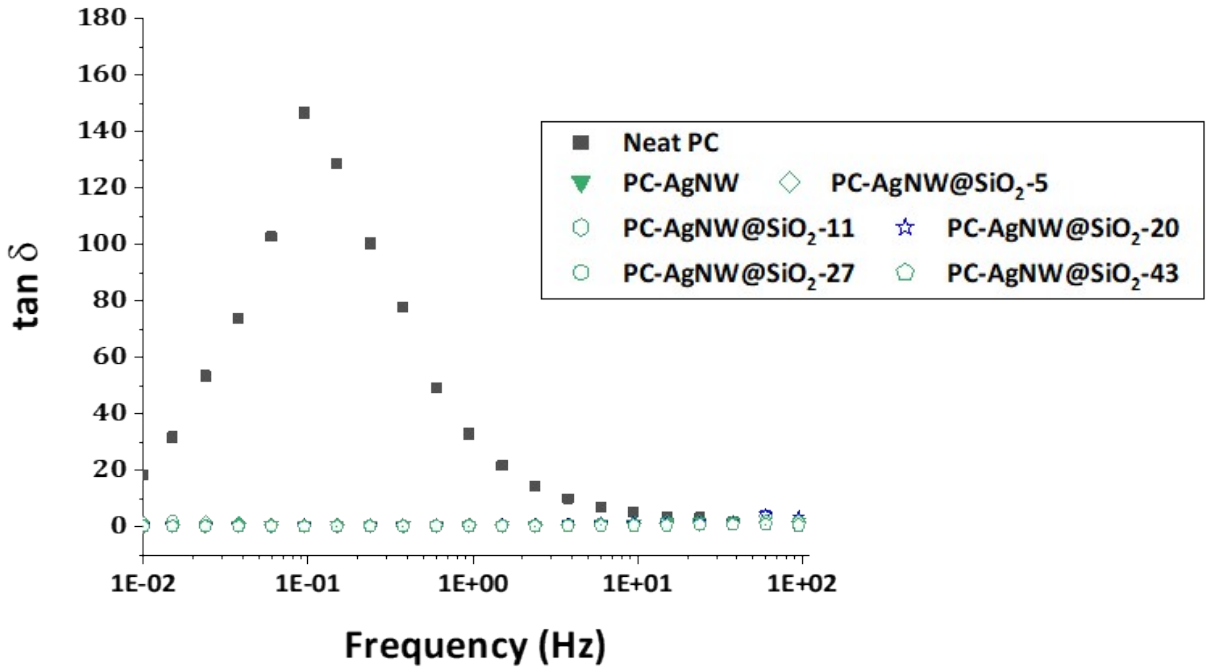

Fig. S13. Variations of tan δ (G"/G') as a function of frequency of neat PC and PC nanocomposites at 250 °C.

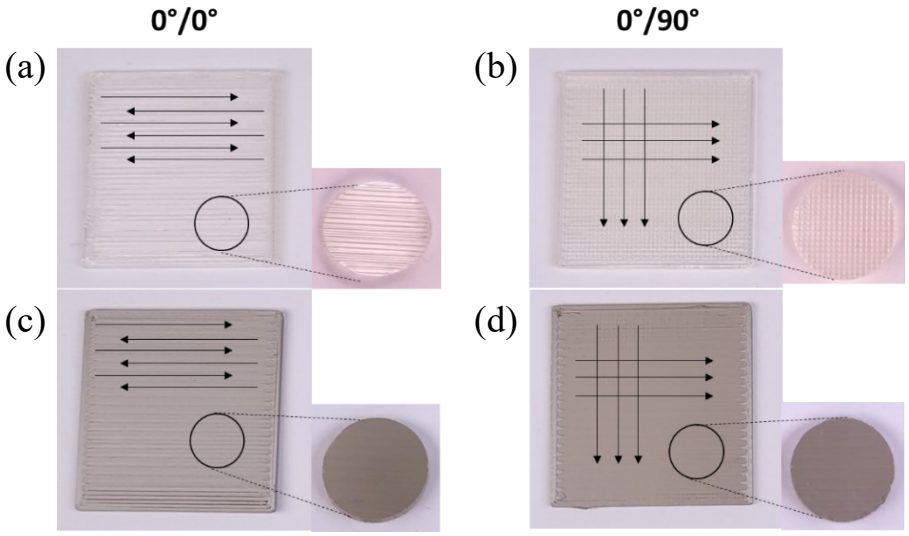

Fig. S14. 3D printed test specimens: (a-b) neat PC and (c-d) PC-AgNW@SiO2-20. (a) and (c) are printed with a unidirectional 0/0 rectilinear infill while (b) and (d) are printed with a criss crossed 0/90 rectilinear infill.

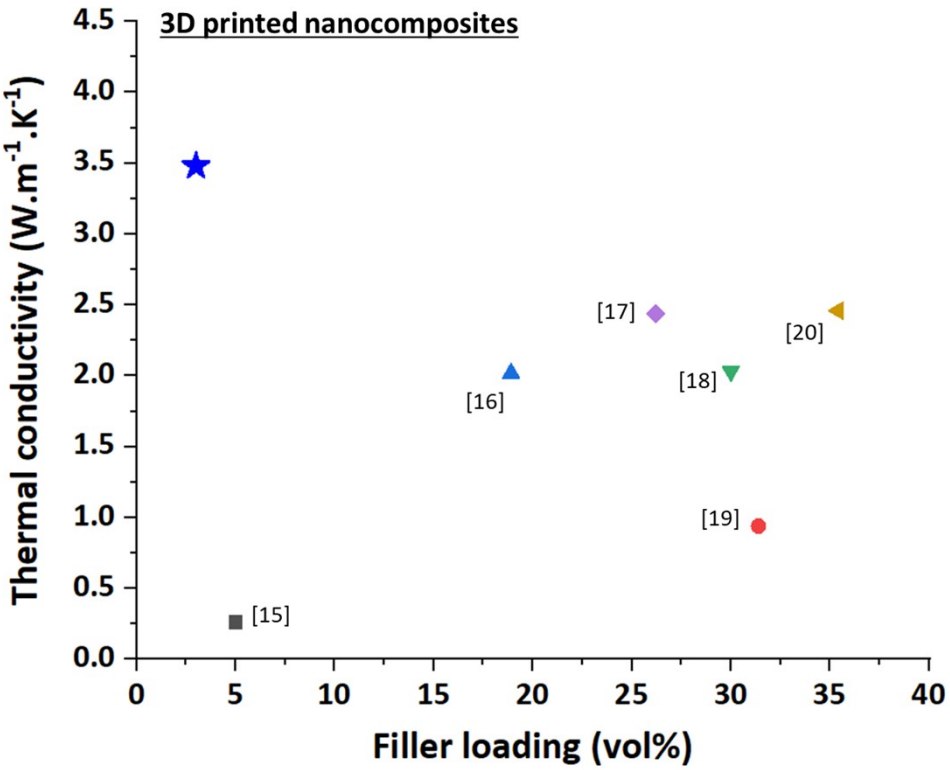

Fig. S15. Thermal conductivity values issued from the literature for 3D printed, thermally conductive and electrically insulating polymer nanocomposites, compared to this work (blue star). References are the following:

[15] Akintola TM, Tran P, Sweat RD, Dickens T. Thermomechanical Multifunctionality in 3D-Printed Polystyrene-Boron Nitride Nanotubes (BNNT) Composites. J Compos Sci 2021;5:61. https://doi.org/10.3390/jcs5020061.

[16] Li J, Leng J, Jiang Y, Zhang J. Experimental characterization of 3D printed PP/h-BN thermally conductive composites with highly oriented h-BN and the effects of filler size. Composites Part A: Applied Science and Manufacturing 2021;150:106586. https://doi.org/10.1016/j.compositesa.2021.106586.

[17] Liu J, Li W, Guo Y, Zhang H, Zhang Z. Improved thermal conductivity of thermoplastic polyurethane via aligned boron nitride platelets assisted by 3D printing. Composites Part A: Applied Science and Manufacturing 2019;120:140–6. https://doi.org/10.1016/j.compositesa.2019.02.026.

[18] Geng Y, He H, Jia Y, Peng X, Li Y. Enhanced through-plane thermal conductivity of polyamide 6 composites with vertical alignment of boron nitride achieved by fused deposition modeling. Polymer Composites 2019;40:3375–82. https://doi.org/10.1002/pc.25198.

[19] Waheed S, Cabot JM, Smejkal P, Farajikhah S, Sayyar S, Innis PC, et al. Three-Dimensional Printing of Abrasive, Hard, and Thermally Conductive Synthetic Microdiamond–Polymer Composite Using Low-Cost Fused Deposition Modeling Printer. ACS Appl Mater Interfaces 2019;11:4353–63. https://doi.org/10.1021/acsami.8b18232.

[20] Wang J, Mubarak S, Dhamodharan D, Divakaran N, Wu L, Zhang X. Fabrication of thermoplastic functionally gradient composite parts with anisotropic thermal conductive properties based on multicomponent fused deposition modeling 3D printing. Composites Communications 2020;19:142–6. https://doi.org/10.1016/j.coco.2020.03.012.

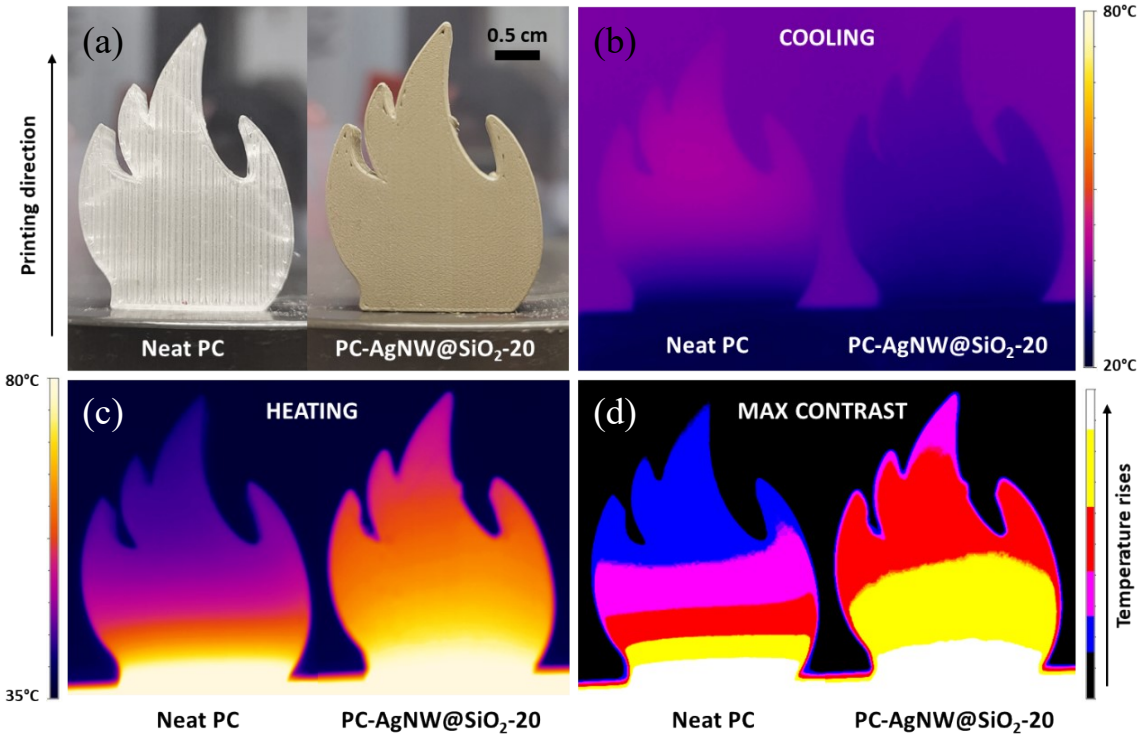

Fig. S16. (a) Pictures of 3D printed demo parts of neat PC and PC-AgNW@SiO_2-20 with corresponding thermal images during (b) cooling and (c) heating cycles after 150 s from t_0; (d) highlighting of the thermal gradients through thermal images of printed parts during a heating cycle using the max contrast tool.

Table S1. Through-plane and in-plane thermal conductivities of various materials along with their respective thermal conductivity enhancement over neat PC at 25 °C.

Materials	**Through-plane** thermal conductivity $\lambda_{\perp}$ ($W.m^{-1}.K^{-1}$)	**In-plane** thermal conductivity $\lambda_{//}$ ($W.m^{-1}.K^{-1}$)
Neat PC	0.23 ± 0.01	0.23 ± 0.01
PC-AgNW	0.42 ± 0.01 *+82%*	0.73 ± 0.02 *+213%*
PC-AgNW@SiO_2-5	0.62 ± 0.03 *+168%*	1.82 ± 0.04 *+683%*
PC-AgNW@SiO_2-11	0.65 ± 0.04 *+183%*	1.98 ± 0.04 *+753%*
PC-AgNW@SiO_2-20	0.66 ± 0.03 *+186%*	2.08 ± 0.05 *+800%*
PC-AgNW@SiO_2-27	0.66 ± 0.01 *+185%*	2.02 ± 0.05 *+768%*
PC-AgNW@SiO_2-43	0.62 ± 0.01 *+167%*	1.82 ± 0.04 *+686%*

Table S2. Tensile properties of neat PC, PC-AgNW and PC-AgNW@SiO_2-20

Materials	Young's modulus (GPa)	Tensile strength (MPa)	Elongation at break (%)
Neat PC	2.01 ± 0.13	66.5 ± 2.5	6.0 ± 0.6
PC-AgNW	2.27 ± 0.04	20.4 ± 2.9	1.0 ± 0.2
PC-AgNW@SiO_2-20	2.60 ± 0.09	44.5 ± 2.4	2.1 ± 0.2

Table S3. In-plane thermal conductivity of various thermally conductive and electrically insulating (> 10^9 Ω cm) 3D printed (nano)composites by FDM from the literature compared to our work.

FDM 3D printed materials (matrix-filler)	Loading (vol%)*	Thermal Conductivity (W m^{-1} K^{-1})**	Ref.
PS-BNNT	5.0	0.26	[15]
PP-hBN	18.9	2.02	[16]
TPU-hBN	26.2	2.44	[17]
PA6-hBN	30.0	2.03	[18]
ABS-microdiamonds	31.4	0.94	[19]
PCL-hBN	35.4	2.46	[20]
PC-AgNW@SiO_2	3.0	3.48	This work

**calculated from wt%, **parallel to the printing direction*